


Article

Weak Multiple Fault Detection Based on Weighted Morlet Wavelet-Overlapping Group Sparse for Rolling Bearing Fault Diagnosis

Wan Zhang ^{1,*} , Yu Ding ¹, Xiaoan Yan ² and Minping Jia ³

¹ Department of Automation, Nanjing University of Information Science and Technology, Nanjing 210044, China; dingyu@nuist.edu.cn

² School of Mechanical and Electronic Engineering, Nanjing Forest University, Nanjing 210037, China; yanxiaoan89@sina.com

³ School of Mechanical Engineering, Southeast University, Nanjing 211102, China; mpjia@seu.edu.cn

* Correspondence: zhangwan@nuist.edu.cn; Tel.: +86-1585-185-8693

Received: 14 December 2019; Accepted: 11 March 2020; Published: 18 March 2020



Abstract: As one of the important parts of a mechanical transmission system, a rolling bearing often has multiple faults coexisting, and the mutual coupling between multiple faults poses a challenge for accurate diagnosis of rolling bearings. Aiming at the above problems, this paper proposes a weighted Morlet wavelet-overlapping group sparse (WOGS) algorithm for the multiple fault diagnosis of rolling bearings. On the basis of the overlapping feature of Morlet wavelet transform coefficients, a WOGS optimization model was initially constructed. Thereafter, the weight coefficients in the model were constructed by analyzing the impulse features of the signal. Thus, majorization-minimization was used to solve the optimization problem. A case study on weak multiple fault diagnosis of rolling bearings was performed to validate the effectiveness of the WOGS algorithm. Quantitative indexes are used to further discuss the extraction accuracies of different algorithms, and the results show that the proposed algorithm exhibits better performance than other algorithms.

Keywords: overlapping group sparse; multiple fault diagnosis; morlet wavelet transform; rolling bearing; sparse optimization

1. Introduction

Rolling bearings act as tiny transmission components in a complex mechanical system. If a rolling bearing fails, then the overall failure rate of a complex system will increase due to its scale effect, which will cause significant economic losses or serious safety accidents [1]. Rolling bearings often have multiple faults coexisting, and multiple fault features are coupled with one another in real industries. Compared with a single fault, the coupling between multiple faults makes fault diagnosis more difficult. In order to solve these problems, various methods—vibration analysis [2–4], current signal signature analysis [5], acoustic emission feature recognition [6], etc., are widely used in rolling bearing fault diagnosis. Because a vibration signal directly expresses the dynamic behavior of the faulty bearing and is sensitive to faults, it has been widely used in industry.

As a core concept of condition monitoring and fault diagnosis, a signal processing technique is an efficient and effective method for fault feature extraction. Take as examples, empirical mode decomposition (EMD) [2,7,8], wavelet transform [9,10], spectral kurtosis [3,11], stochastic resonance [12],

and morphological filtering [13]. The above traditional signal processing methods are suitable for the feature extraction of a single fault; hence, they are generally inapplicable to multiple fault diagnosis. Therefore, some improved algorithms have been proposed for multiple fault diagnosis. Jiang et al. [14] used multiwavelet packets as pre-filters to improve colored ensemble empirical mode decomposition (EEMD) results and the improved algorithm to analyze the multiple faults in a rotor experimental device and industrial machine set. Chen et al. [15] combined an improved adaptive redundancy lifting multiwavelet with a Hilbert transform algorithm for rolling bearing compound fault detection. Furthermore, Zhang et al. [16] proposed a method on the basis of resonance sparse decomposition and comb filter for gearbox multiple fault diagnosis. The proposed method achieves composite fault separation on the basis of the morphological differences of divergent types of faults. Du et al. [17] proposed a sparse feature recognition method on the basis of the union of redundant dictionary for multiple fault diagnosis with different morphological waveforms.

The above fault separation methods obtain effective results in multiple fault diagnosis, but they still suffer from the following drawbacks. (1) The methods based on EMD [2,7,8], wavelet transform [9,10], and spectral kurtosis [3,11] are used to construct the appropriate filter to extract the resonance band where the local fault is located. Since a single local fault has only one resonance band in the frequency domain, it is easy to extract fault features by constructing an appropriate filter. However, under complex faults, the resonance band information is more complex, so it is difficult to achieve the ideal effect simply by constructing band-pass filter. (2) The morphological method can realize multiple faults separation, which is based on different fault signals with different morphological characteristics. For example, the morphological method can successfully separate the harmonic morphology and periodic impulsive waveforms in [17], which respectively indicate the misalignment of the gearbox output shaft and localized faults in a gear. In the multiple faults of rolling bearings, such as inner and outer faults, the fault features are all in the form of impulse, and the morphological difference is small. Therefore, obtaining the desired effect by using the difference in fault features to separate the multiple faults of rolling bearings is difficult.

Different from the above methods, sparse representation can effectively realize the capture of the essence of information and the most efficient expression. The method based on sparse representation has been widely used in the field of mechanical fault diagnosis [18–22]. For instance, Yang et al. [23] used basis pursuit to diagnose rolling bearing faults. The result shows that the basis pursuit can represent features with fine resolution in the time-frequency domain, which makes explaining the fault features easy. Feng and Chu [24] applied some typical atomic decomposition methods, such as the method of frames, best orthogonal basis, and matching and basis pursuits, to analyze the vibration signals of damaged gearboxes. Moreover, Liu et al. [25] used the matching pursuit and time-frequency atom to analyze the bearing vibration signals and extract the vibration signatures.

In recent years, structural group sparse methods have received extensive attention in the fields of statistics, machine learning, signal processing, computer vision, and biological information [26–29]. Structural group sparse indicates not only that the signal is sparse, but also that the signal has a simple form of structural sparsity [30]. Group sparsity can be divided into non-overlapping group sparse and overlapping group sparse models. If no coupling exists between adjacent groups in the signal, then constructing a non-overlapping group sparse model can simplify the optimization problem [31]. Non-overlapping group sparse is often not satisfactory to obtain good noise reduction results; therefore, the overlapping group sparse (OGS) model is introduced. For instance, OGS has been implemented for estimating sparse signals in noise [32]. OGS is a special structure in the structural group sparse model, indicating that an overlap exists between adjacent groups. In addition to the sparsity of the wavelet coefficients of the multiple fault features, interrelated structures also exist between the coefficients. OGS has been introduced to the field of fault diagnosis in recent years. For instance, on the basis of the overlapping group shrinkage and majorization-minimization (MM), He et al. [33,34] extracted the periodic

group sparse signal from the vibration signal and realized the compound fault diagnosis of rolling bearings. The proposed algorithm requires a priori knowledge of the location of the fault to further separate the different faults. OGS is an effective method for extracting compound faults. However, the following problems also exist. (1) Determining the location of the fault before disassembling is impossible. (2) The literature [33,34] is based on the prior knowledge of the sparsity of the fault signal itself, but the fault signal is sparse under wavelet transform, and the signal itself is not sparse. In this research, OGS is improved to overcome these shortcomings.

In industry, during the degradation of a bearing, multiple types of faults may coexist, and the signal is weak due to the long signal transmission path. Therefore, in this research, a multiple fault feature extraction method based on the WOGS is proposed. Overlaps emerge in the time domain due to the different types of faults; thus, the wavelet transform coefficients must also overlap. The OGS model is constructed on the basis of the overlapping wavelet transform coefficients, and the sparse model is solved by MM. The weight coefficients in the OGS model are then estimated by analyzing the salient features of the vibration signal. Consequently, the weak impulse features in the vibration signal can be enhanced, which are then evaluated for multiple fault diagnosis.

The rest of this paper is organized as follows. In Section 2, the OGS is reviewed and the majorization-minimization algorithm for the OGS problem is presented. Section 3 details the proposed algorithm to extract multiple fault features. Section 4 covers the verification of the proposed algorithm by using a simulated signal model. Section 5 presents the experimental study to further validate the proposed algorithm. Finally, Section 6 concludes the paper.

2. Background

2.1. Overlapping Group Sparse

The observed vibration signal of rolling bearing y is denoted as $y = [y(0), \dots, y(n - 1)]^T$ in R^n , which is described as:

$$y(i) = x(i) + w(i), i \in I. \tag{1}$$

where the signal $x(\in R^n)$ is known to have a group property, and $w(\in R^n)$ is white Gaussian noise. According to the prior knowledge that x has group sparse characteristics, a sparse component x can be solved from the observed signal y by establishing a sparse optimization model:

$$\hat{x} = \arg \min_x \left\{ F(x) = \frac{1}{2} \|y - x\|^2 + \lambda G(x) \right\}. \tag{2}$$

where $\lambda > 0$ is the regularization parameter. The first addend in (2) is the fidelity term, which can constrain the error between the estimated signal \hat{x} and the observed signal y . The second addend is the penalty term, which can constrain the sparsity of x . The parameter λ is used to balance the constraint weight between the fidelity term and the sparse term. In addition, non-zero coefficients usually are not independently distributed and form a cluster, and the overlaps of coefficients emerge between adjacent groups. Therefore, the overlapping group lasso function can be selected to build regularization term $G(x)$, which is defined as:

$$G(x) = \sum_{i \in I} \left[\sum_{j \in J} |x(i + j)|^2 \right]^{1/2}, \tag{3}$$

where i is the group index, j is the index of the coefficients in group i , and each group is of the same size $|J|$. For a one-dimensional signal x of length N and group size K , we set I in Equation (3) to:

$$I = \{0, \dots, N - 1\}. \tag{4}$$

and J in Equation (3) is set to:

$$J = \{0, \dots, K - 1\}. \tag{5}$$

In the rolling bearing multiple fault, because different fault features have overlapping features in the time-domain, their wavelet transform coefficients also have the feature of overlapping sparse groups. If a non-overlapping group sparse model is used to build a model with overlapping group sparse, it will lead to the problem of missing partial coefficients. In the following, from the perspective of the selection of overlapping group sparse coefficients between non-overlapping group sparse model and overlapping group sparse model, it shows that the overlapping group model is more suitable for coefficient selection with the overlapping group sparse property. Figure 1 shows that coefficients have overlapping group structure, where each ellipse represents a group. Group x_3, x_4, x_5, x_6 and group x_{10}, x_{11} are selected, and other groups are discarded; meanwhile, coefficients x_3 and x_4 are overlapping parts. Coefficient selection results of non-overlapping group sparse model are shown in Figure 2a; the coefficients of the overlapping part x_3 and x_4 will eventually be discarded. If the overlapping group sparse model is used, the result of coefficient selection is shown in Figure 2b, and the overlapping parts x_3 and x_4 will be retained eventually.

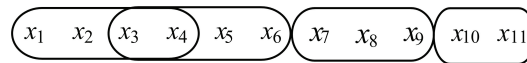


Figure 1. Coefficients with overlapping group structure.

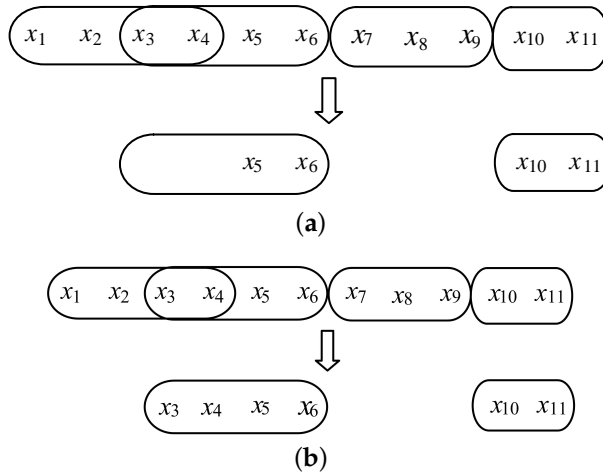


Figure 2. Coefficient selection results: (a) non-overlapping group sparse; (b) overlapping group sparse.

2.2. Majorization-Minimization for OGS

The solution of the sparse optimization problem is usually divided into two steps. The first step is to pre-process the objective function, and transform the objective function that is non-smooth, non-convex, and inseparable into a smooth, convex, separable function. The second step is to solve the transformed objective function. MM is suitable for solving difficult optimization problems directly, such as non-differentiable problems. MM does not need to directly minimize the objective function $F(x)$ in Equation (2), but converts $F(x)$ into optimization problem $Q_k(x, x_k), \{k = 0, 1, 2, \dots\}$. The advantage of this is that the solution of $Q_k(x, x_k)$ is simpler than optimization problem $F(x)$. The constructed function $Q_k(x, x_k)$ needs to satisfy the following constraints:

$$\begin{cases} Q_k(x, x_k) \geq F(x), \forall x \\ Q_k(x_k, x_k) = F(x_k) \end{cases} \tag{6}$$

Through the k -th iterations, $Q_k(x, x_k)$ converges to the minimum value of the objective function $F(x)$. Because the MM method is simple to use and efficiently calculated, it plays a more prominent role in multivariable optimization. Using MM algorithm to solve the optimization function $F(x)$ can be summarized as the following steps:

- (1) Construct an appropriate function $Q_k(x, x_k)$ to satisfy the constraints in Equation (51);
- (2) Calculate the minimum of $Q_k(x, x_k)$, marked as x_{k+1} :

$$x_{k+1} = \arg \min_x Q_k(x, x_k); \tag{7}$$

- (3) Let $k = k + 1$; go to step (2).

To solve the sparse optimization problem (2), we use the MM algorithm. For instance, if the group size is set to $K = 2$, then the optimization objective function $F(x)$ in Equation (2) is expanded as:

$$F(x) = \min_{\theta \in \mathbb{R}^N} \frac{1}{2} \|y - x\|^2 + \lambda \left(\dots + \sqrt{|x(1)|^2 + |x(2)|^2} + \sqrt{|x(2)|^2 + |x(3)|^2} + \sqrt{|x(3)|^2 + |x(4)|^2} + \dots \right) \tag{8}$$

The derivative is expressed as:

$$\frac{\partial F(x)}{\partial x(i)} = x(i) - y(i) + \lambda x(i) \left(\frac{1}{\sqrt{|x(i-1)|^2 + |x(i)|^2}} + \frac{1}{\sqrt{|x(i)|^2 + |x(i+1)|^2}} \right), 0 \leq i \leq N - 1. \tag{9}$$

In Equation (9), $x(-1)$ and $x(N)$ can be considered zero, as noted for $i \notin I$. The Equation (9) is rewritten as:

$$\frac{\partial F(x)}{\partial x(i)} = x(i) - y(i) + \lambda x(i)r(i; x), \tag{10}$$

where $r(i; x) = \sum_{j \in J} \left[\sum_{k \in J} |x(i - j + k)|^2 \right]^{-1/2}$.

Setting the derivative to zero, we can formulated the optimization problem as:

$$x(i) + \lambda x(i)r(i; x) = y(i), i \in I. \tag{11}$$

Hence, rewrite Equation (11) as:

$$x(i) = \frac{y(i)}{1 + \lambda r(i; x)}, i \in I. \tag{12}$$

More details about the MM procedure can be found in [35,36].

3. The Proposed Algorithm

3.1. WOGS Model

Fault signal x is assumed to be non-sparse, but it is approximately sparse under the Morlet wavelet transform. Fault signal x can be expressed as:

$$x = \Phi\theta, \tag{13}$$

where Φ and θ represent the Morlet wavelet dictionary and the sparse representation coefficient. In order to solve the regularization inverse problem, that is, recover x from the observed vibration signal y , the sparse optimization problem can be formulated as:

$$\theta^{opt} = \arg \min_x \left\{ F(\theta) = \min_{\theta \in \mathbb{R}^N} \frac{1}{2} \|y - \Phi\theta\|^2 + \lambda G(\theta) \right\}, \tag{14}$$

where $G(\theta)$ is a regularized penalty function for inducing sparse solutions. Penalty term $G(\theta)$ depends on the structural form of coefficient θ . In the multiple fault signal of rolling bearings, only a small number of coefficients have large amplitudes, and the rest are close to zero. The OGS regularization term in Equation (3) is used to characterize the overlapping group sparsity of x . Therefore, the regularization function based on the Morlet wavelet transform coefficient θ is defined as

$$G(\theta) = \sum_i \left[\sum_{j \in J} |\theta(i+j)|^2 \right]^{1/2} \tag{15}$$

for a two-dimensional (2-D) vector (θ) of size $N_1 \times N_2$ with a group size of $K_1 \times K_2$, and then I and J are set to:

$$I = \{(i_1, i_2) : 0 \leq i_1 \leq N_1 - 1, 0 \leq i_2 \leq N_2 - 1\}, J = \{(j_1, j_2) : 0 \leq j_1 \leq K_1 - 1, 0 \leq j_2 \leq K_2 - 1\}. \tag{16}$$

3.2. Adaptive Weight Parameter

The value of the weights w_i in the OGS problem have a great effect on the accuracy of fault feature extraction. In view of this dependence on the weight selection, the weights w_i are constructed by analyzing the salient features of the fault signals. The purpose of modifying the values of the weights is to obtain a good reconstruction of the impulse signal. Introducing the corrected weights to penalty item $G(\theta)$ can be written as follows:

$$G(\theta) = \sum_{i=1}^n w_i \|\theta_{i,K}\|_2 \tag{17}$$

$k \in \text{supp}(y)$ should denote the position of the significant feature, such as the impulse sequence; $\tilde{\Gamma}_k \subset \Gamma$ should be the set of groups containing position k ; and finally, define a shrinkage operator on the weights $P : w \in R_+ \rightarrow R_+$ by:

$$P(w_i) \equiv \tilde{w}_i = \begin{cases} a_i w_i & \text{if } g(i) \in \tilde{\Gamma}_k \\ w_i & \text{otherwise} \end{cases} \tag{18}$$

where $a_i \in [0; 1]$. For the given group $g(i)$, if $\tilde{w}_i \leq w_i$, then the weights are correspondingly weakened in the optimization process. Therefore, preserving the coefficients of the fault-related salient features during the regularization process is advantageous.

$|\theta_{j,n}|$ should be the wavelet coefficient at position n and scale j under the Morlet wavelet transform. The normalized wavelet coefficients can be written as:

$$\delta(n) := \left(\prod_{j=J_0}^J \gamma(|\theta_{j,n}|) \right)^{1/(J-J_0+1)} \tag{19}$$

where $\gamma(\cdot)$ is expressed as

$$\gamma(\theta_{j,n}) = \frac{\theta_{j,n} - \min \theta_{j,\cdot}}{\max \theta_{j,\cdot} - \min \theta_{j,\cdot}} \tag{20}$$

In (20), $\gamma(\cdot)$ denotes the normalization function. At the location of the impact sequence, the normalized wavelet coefficients δ are close to 1. When the signal is in the smoothing phase, the normalized wavelet coefficients δ are approximately zero. Threshold and the minimum interval length of r are defined to find the location of the impulse points. We define set $K_{\tau,r}(1), K_{\tau,r}(2), K_{\tau,r}(S)$ as a non-empty, disjoint, non-adjacent interval that must satisfy the interval length greater than r and $\delta(n) > \tau$. The position of the salient feature in the observed signal y is determined by the S set of positions $K_{\tau,r}$ in the following equation:

$$K_{\tau,r} := \left\{ \max_{n \in K_{\tau,r}(s)} \delta(n) \right\}_{s=1}^S \tag{21}$$

Algorithm 1 gives the process of estimating the set of positions $K_{\tau,r}$ and the value of weights $\{w_i\}$, which are determined by the choice of parameters τ and r .

Algorithm 1: Determination of the set of positions $K_{\tau,r}$ and adaptive weights $\{w_i\}$.

Input: $y; r, n_0$

Output: $\{w_i\}$

Procedure:

$\theta \leftarrow \text{MorletCWT}(y)$

$\delta(n) \leftarrow \theta$

$\{\tau_q\} \leftarrow \delta$

$K_{\tau_q,r} \leftarrow \{n : \delta(n) > \tau_q\}$

$K_{\tau_q,r}(i) \leftarrow \arg \max_{n \in K_{\tau_q,r}(i)} \delta(n)$

$\tilde{\Gamma}_k \leftarrow K_{\tau_q,r}$

$\hat{\sigma}^2 \leftarrow \text{Estimate noise variance from } \theta$

$a \leftarrow \text{Set shrinkage factor according to } \hat{\sigma}$

$\{w_i\} \leftarrow (\tilde{\Gamma}_k, a)$

End

3.3. The Fault Feature Extraction Algorithm Based on WOGS

When the fault signal x itself has overlapping group sparsity characteristics, the optimal solution is obtained by using Equation (12). However, the actual fault signal does not have sparsity characteristics, and the multi-fault signal has overlapping group sparsity characteristics under wavelet transform, so the WOGS problem is constructed, as shown in Equation (14). Similarly, MM algorithm is used to solve the WOGS problem, and the derivative of Equation (14) is expressed as:

$$\frac{\partial F(\theta)}{\partial \theta(i)} = \Phi^{-1}(\Phi\theta(i) - y(i)) + \lambda\theta(i)r(i;\theta) \tag{22}$$

where $r(i;\theta) = \sum_{j \in J} \left[\sum_{k \in J} |\theta(i - j + k)|^2 \right]^{-1/2}$ Hence, the optimal $\theta(i)$ can be obtained:

$$\theta(i) = \frac{\Phi^{-1}y(i)}{1 + \lambda r(i;\theta)}, i \in I. \tag{23}$$

The fault signal x is reconstructed according to the wavelet transform coefficients:

$$x = \Phi\theta \tag{24}$$

The fault feature extraction algorithm based on WOGS is summarized in Algorithm 2. Moreover, its corresponding flow chart is shown in Figure 3.

Algorithm 2: Fault feature extraction based on WOGS.

- 1: Input: y, w, K .
- 2: Initialize morlet-wavelet transform coefficient: $\theta = \Phi^{-1}y$.
- 3: Construct 2-D MW-OGS optimization problem: $\theta^{opt} = \arg \min_x \left\{ F(\theta) = \min_{\theta \in \mathbb{R}^N} \frac{1}{2} \|y - \Phi\theta\|^2 + \lambda G(\theta) \right\}$.
- 4: Calculate weight coefficient: $\{w_i\} \leftarrow (\tilde{\Gamma}_k, a)$.
- 5: Solve WOGS problem: $\theta(i) = \frac{\Phi^{-1}y(i)}{1+w_i r(i; \theta)}, i \in I'$.
 Until convergence
- 6: Output denoised signal: $x = \Phi\theta$.
- 7: Envelope demodulation analysis is performed on the denoised signal x to extract fault features.

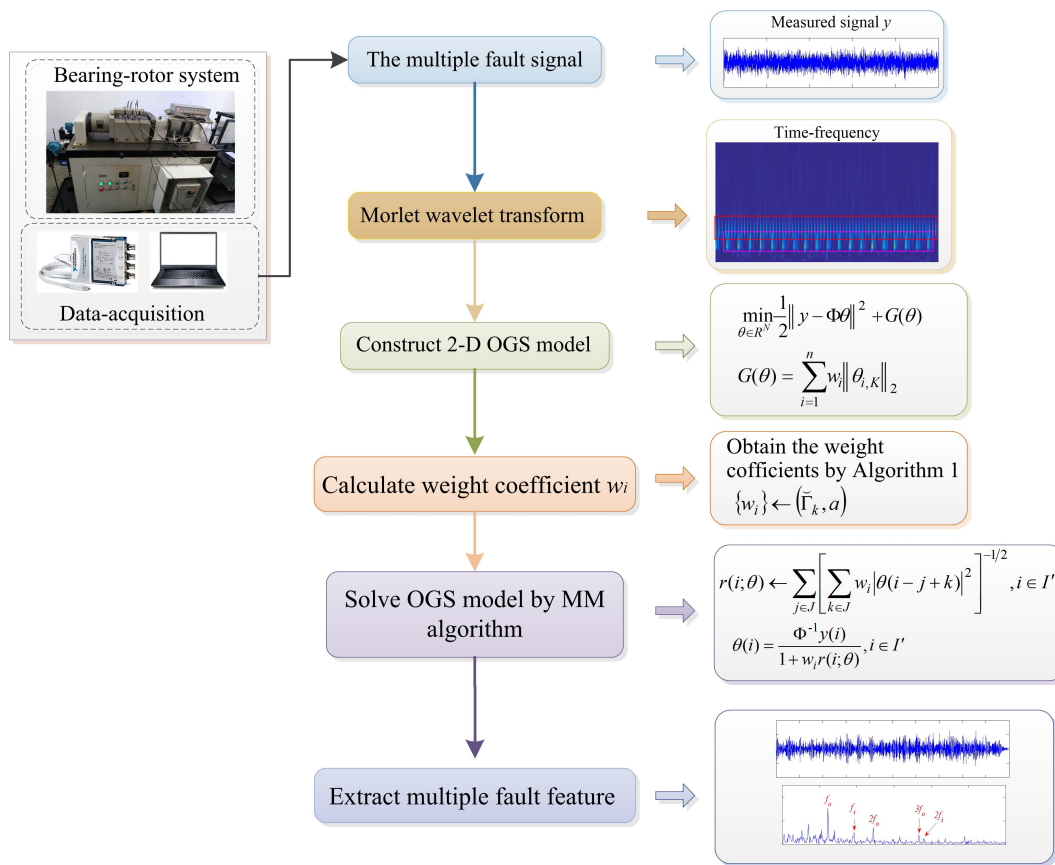


Figure 3. The fault feature extraction algorithm based on WOGS.

4. Simulation Signal Analysis

The actual rolling bearing fault signal model is simplified to verify the effectiveness of the proposed algorithm. Therefore, the simulation model of the rolling bearing multiple fault signal is established:

$$\begin{cases} s(t) = s_1(t) + s_2(t) + w(t) \\ s_1(t) = e^{-80t} \sin(600\pi t) \\ s_2(t) = e^{-250t} \sin(2000\pi t) \end{cases} \quad (25)$$

where $s_1(t)$ is the impulse response caused by the first partial fault with feature frequency $f_1 = 20$ Hz, $s_2(t)$ is the impulse response caused by the second local fault with feature frequency $f_2 = 70$ Hz, and $w(t)$ is white Gaussian noise. The MATLAB script function `awgn(x, SNR)` refers to the addition of white Gaussian noise to the vector signal x . The scalar `snr` specifies the signal-to-noise ratio per sample, in dB. Here, the vector signal is set to $s_1(t) + s_2(t)$, and the signal-to-noise ratio is set to be $SNR = -5$. Figure 4a–c correspond to $s_1(t)$, $s_2(t)$, and $s(t)$, respectively. Seeing the periodic impulse feature from synthesized signal $s(t)$ is difficult. In order to extract periodic impulse features, spectral analysis is a common type of method; such methods include frequency spectral analysis and envelope spectral analysis. Frequency spectrum analysis is used to perform a Fourier transformation on the original signal. Envelope spectrum analysis performs the Hilbert transformation on the original signal, and then the Fourier transform is applied to the envelope. The amplitude of fault feature frequency in the frequency spectrum is small, while the envelope spectrum is sensitive to impulse components, so the amplitude of fault feature frequency in the envelope spectrum is very high and easy to identify. Figure 5 shows the frequency and envelope spectrum of synthesized signal $s(t)$. Figure 5a exhibits that the resonance band corresponding to two local faults, which are marked with red lines. In the envelope spectrum, the frequency components at 20 and 70 Hz have the largest magnitude; they represent the feature frequencies of the two impulses, respectively. In addition to the above feature frequencies, significant noise components are available.

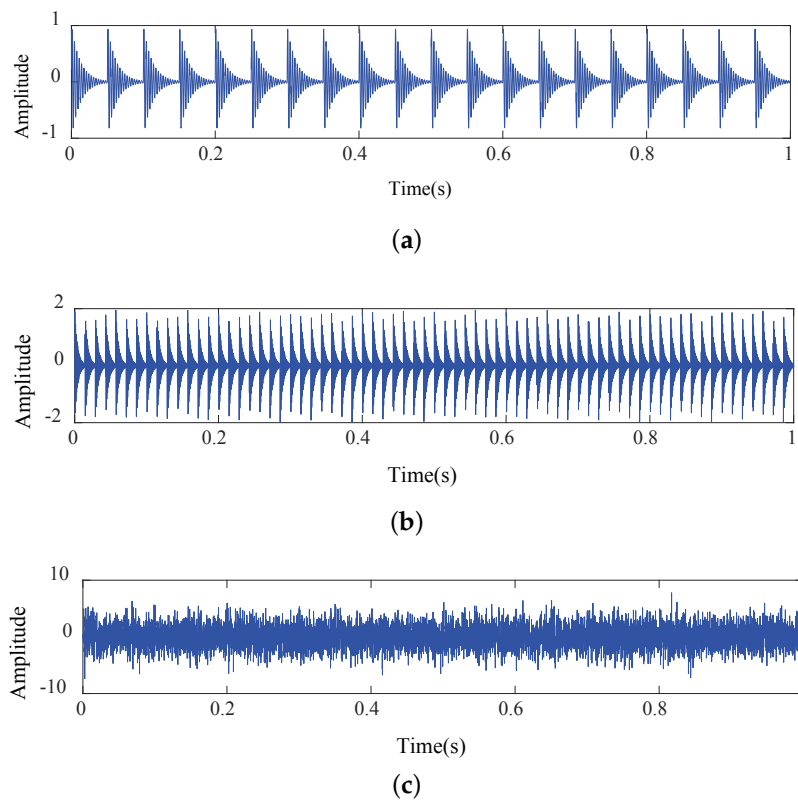


Figure 4. Simulated signal: (a) $s_1(t)$. (b) $s_2(t)$. (c) $s(t)$.

Figure 6 shows the time-frequency representation of the simulated signal based on the Morlet-wavelet transform. As can be seen from the figure, TF_1 and TF_2 correspond to the time-frequency distribution of two local fault signals $s_1(t)$ and $s_2(t)$ in Equation (25), respectively. It can be seen from Figure 6 that they have periodic impact characteristics along the time axis, but it is difficult to get accurate periodic values. The Morlet-wavelet coefficients are taken as the observed signal y in Equation (1). Figure 7a–c shows the denoised results based on the WOGS algorithm with a group size 7×2 (i.e., seven frequency bins \times two time bins). Comparing Figures 5a and 7a, we find that the periodic impulse features are evident after noise reduction. Figure 7b shows the frequency spectrum of the denoised signal, where the two resonance bands representing local faults are preserved. The dominant frequency components in Figure 7c are 20, 40, 60, and 80 Hz, which represent the feature and harmonic frequencies of the first impulse component, and the frequency components at 70, 140, and 210 Hz represent the feature and harmonic frequencies of the second impulse component.

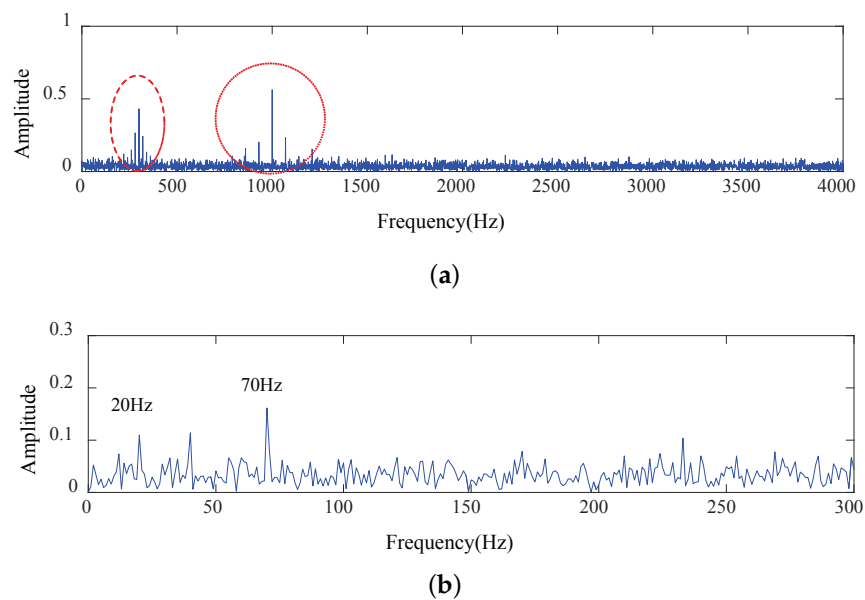


Figure 5. Frequency spectrum and envelope spectrum of the simulated signal: (a) Frequency spectrum of the simulated signal. (b) Envelope spectrum of the simulated signal.

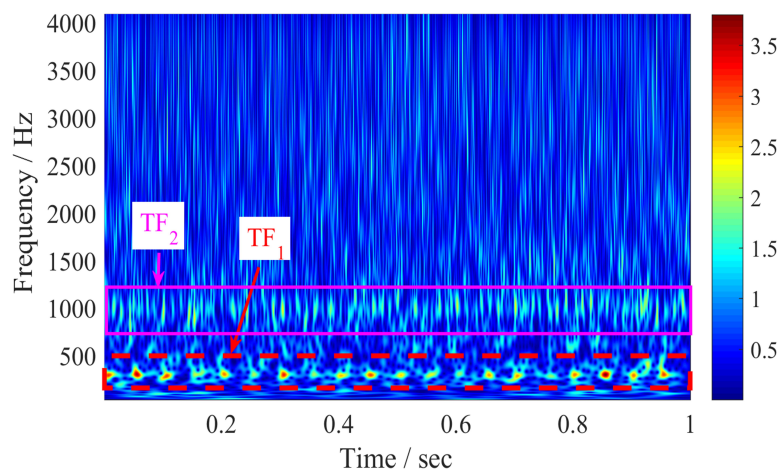


Figure 6. Time-frequency representation of simulated signal.

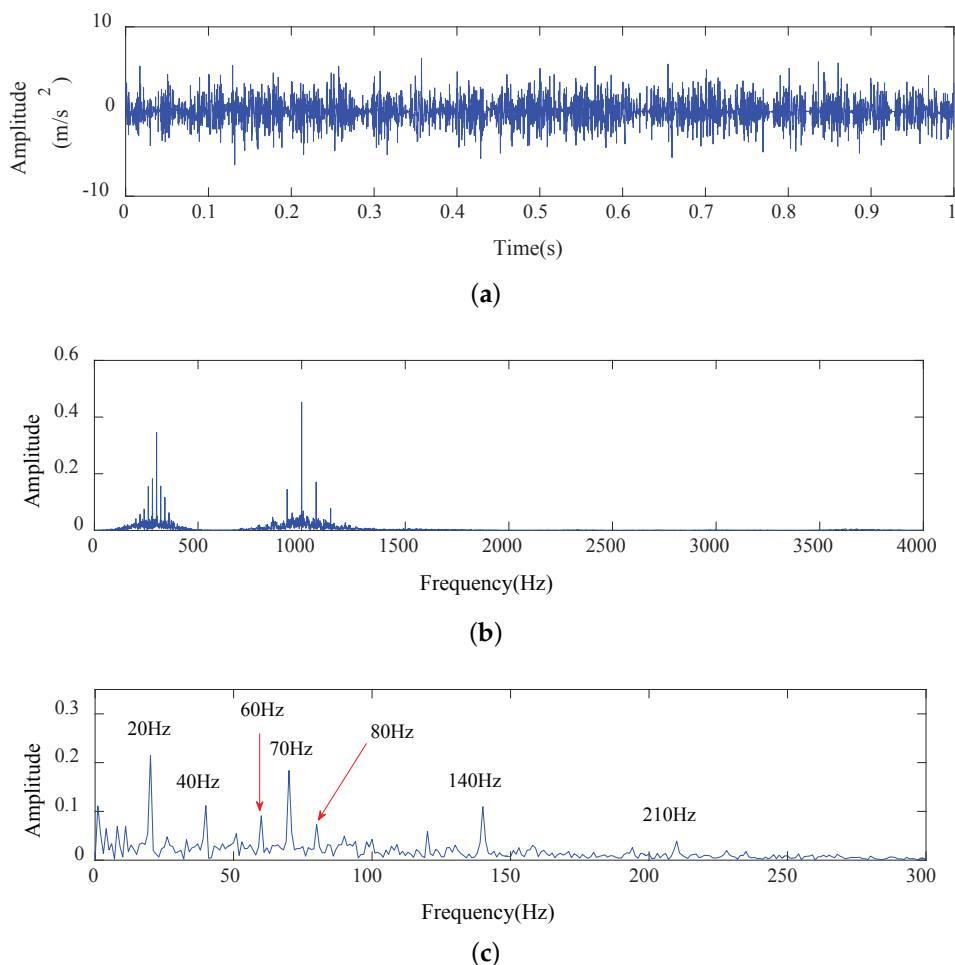


Figure 7. Results of the proposed WOGS algorithm: (a) Time domain waveform. (b) Frequency spectrum. (c) Envelope spectrum.

The simulated signal is decomposed by the tunable Q-factor wavelet transform (TQWT), which is similar to the WOGS algorithm. The sparse optimization model established in TQWT can be written as:

$$\arg \min_{w_1, w_2} \|y - \Phi_1 w_1 - \Phi_2 w_2\| + \sum_{j=1}^{J_1+1} \lambda_{1,j} \|w_{1,j}\|_1 + \sum_{j=1}^{J_2+1} \lambda_{2,j} \|w_{2,j}\|_1 \tag{26}$$

$$x_1 = \Phi_1 w_1 \quad x_2 = \Phi_2 w_2 \tag{27}$$

where Φ_1 and Φ_2 denote the inverse TQWT having high and low Q-factors respectively, and λ_1 and λ_2 are the regularization parameters. The sparse coefficients w_1 and w_2 are obtained by solving the optimization problem. Then, through the signal reconstruction of Equation (25), the high-factors component and low-factors component of the signal can be obtained, which represent the harmonic component and the impact component, respectively. Therefore, TQWT and WOGS have similar ideas for extracting fault features. But based on different prior knowledge, the two algorithms build different models. In order to highlight the weak fault characteristics, we weighted the penalty terms in the WOGS model. The resonance characteristic of the signal is used to construct the wavelet basis in TQWT. However, we use the Morlet wavelet basis function in WOGS. Here, the parameters of the high oscillatory component are $Q_1 = 7$,

$r_1 = 5, J_1 = 10$, and the parameters of the low oscillatory component are $Q_2 = 2, r_2 = 3.5, J_2 = 7$. Figure 8 illustrates the decomposition result of the TQWT, and Figure 8b shows that the impulse feature can be observed in the low oscillatory component. Furthermore, Figure 9a–c exhibits the envelope spectra of the high and low oscillatory and residual components. Figure 9b depicts some obvious peaks at 20 and 70 Hz, corresponding to the feature frequencies of the two different impulse components. The methods in [33,34] use the OGS algorithm to extract multiple faults directly. Figure 10 displays the denoised result of the OGS algorithm with group size $K = 3$. Figure 10 shows that no evident periodic impulse features are available. The same signal was also processed by using soft threshold denoising. Figure 11 shows the denoised results of soft threshold. In addition to the impulse fault frequency, a large amount of noise also emerges.

Compared with other methods that extract multiple fault information when rolling bearing signals are masked by strong noise, the WOGS algorithm can obtain good diagnostic results.

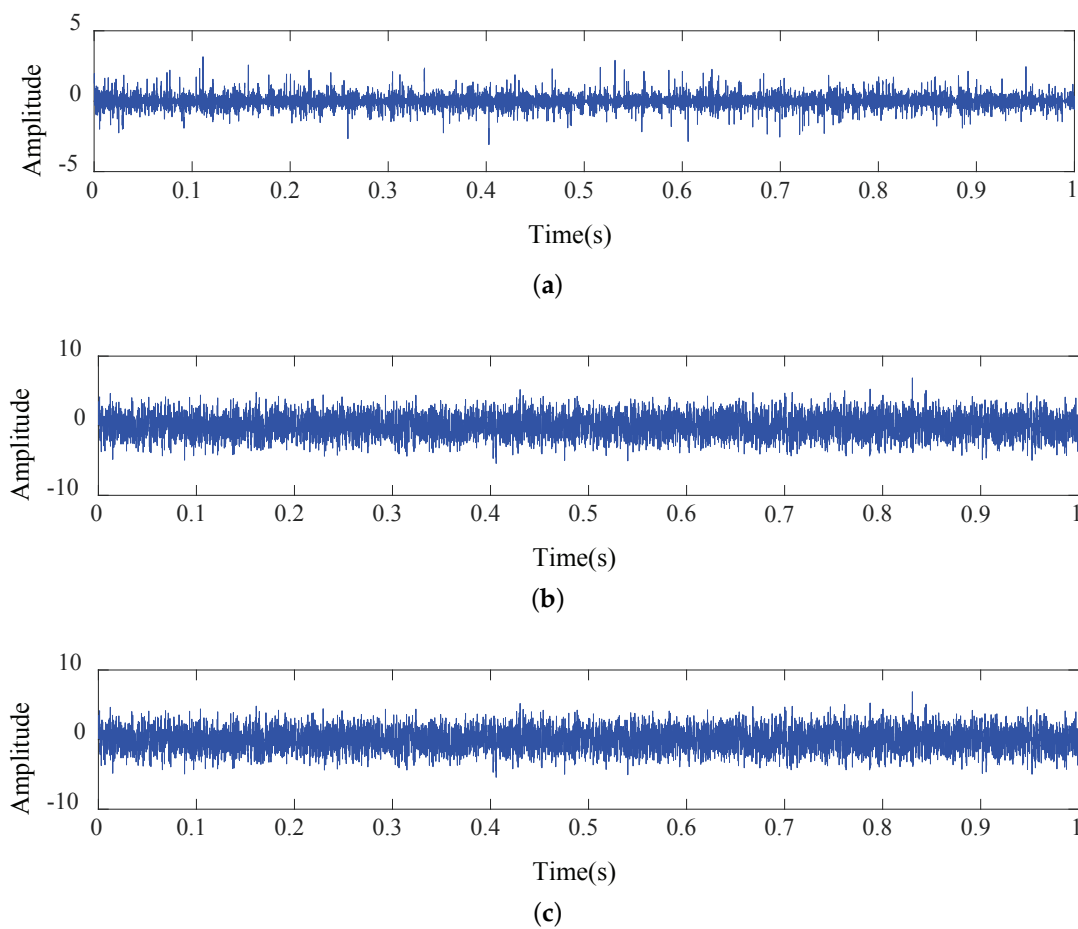


Figure 8. Decomposition results by TQWT: (a) High oscillatory component. (b) Low oscillatory component. (c) Residual component.

The energy ratio at the characteristic frequency is used as an evaluation index to compare the fault feature extraction effects of the above algorithms. The energy ratio can be defined as:

$$R_f = \frac{\sum_{t=1}^4 S(t \times f_i) + \sum_{j=1}^4 S(j \times f_o)}{S(f)} \tag{28}$$

where f_i and f_o correspond to the inner and outer fault characteristic frequencies, respectively. $S(f)$ represents the energy of the entire envelope spectrum. The computer configuration is as follows: the processor—Intel Core i7-8550U; the CPU frequency—1.8 GHz; the memory—16 GB; the graphics card—NVIDIA GeForce MX150; operating system—Win10 (64bit); the program—implemented on MATLAB R2015b. Table 1 shows the energy ratio R_f and CPU running time T_f of the above algorithms. The results show that WOGS algorithm has the largest energy ratio, which indicates that it has a stronger ability to extract weak multiple fault features. However, it is time-consuming to calculate the weight coefficients and Morlet wavelet transform in WOGS algorithm, so the proposed algorithm not only improves the extraction accuracy of the algorithm, but also sacrifices the algorithm efficiency.

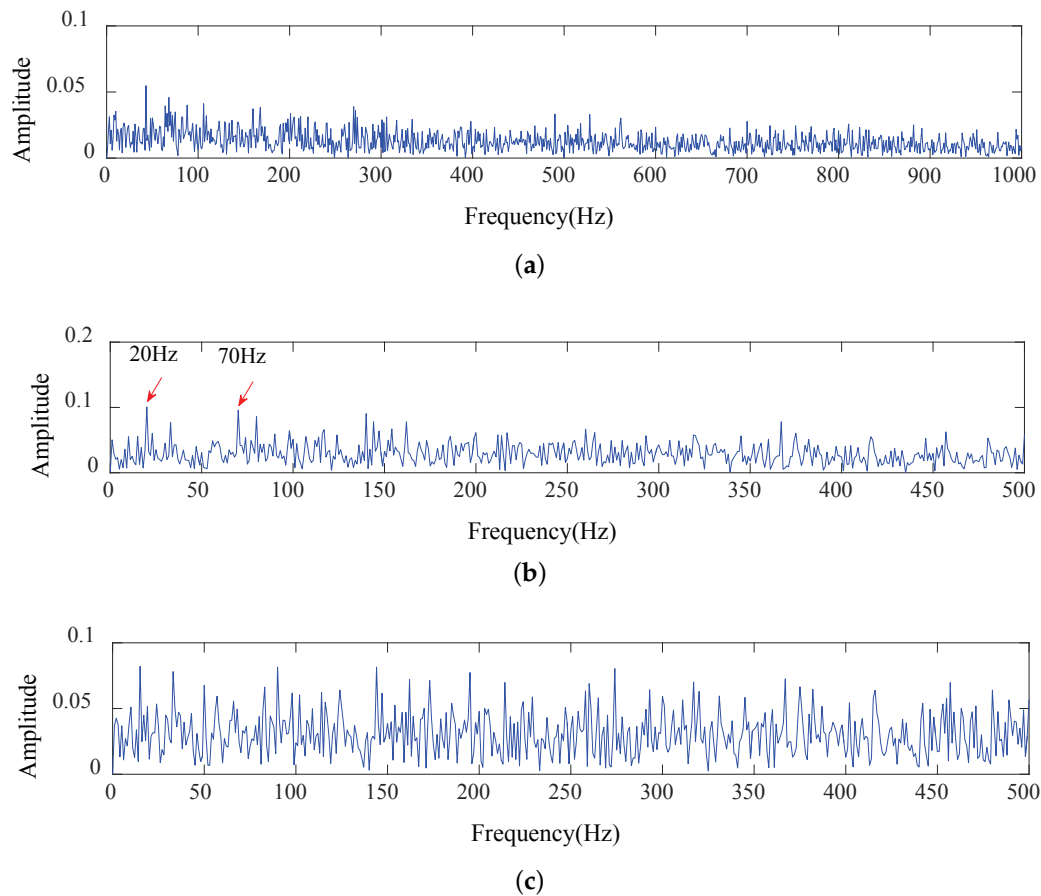


Figure 9. Envelope spectra of the decomposed signals: (a) High oscillatory component. (b) Low oscillatory component. (c) Residual component.

Table 1. Comparison of R_f and T_f of four algorithms.

Algorithms	R_f	$T_f(s)$
TQWT	0.015	1.76
OGS	0.079	1.17
Soft threshold	0.018	0.44
WOGS	0.242	1.40

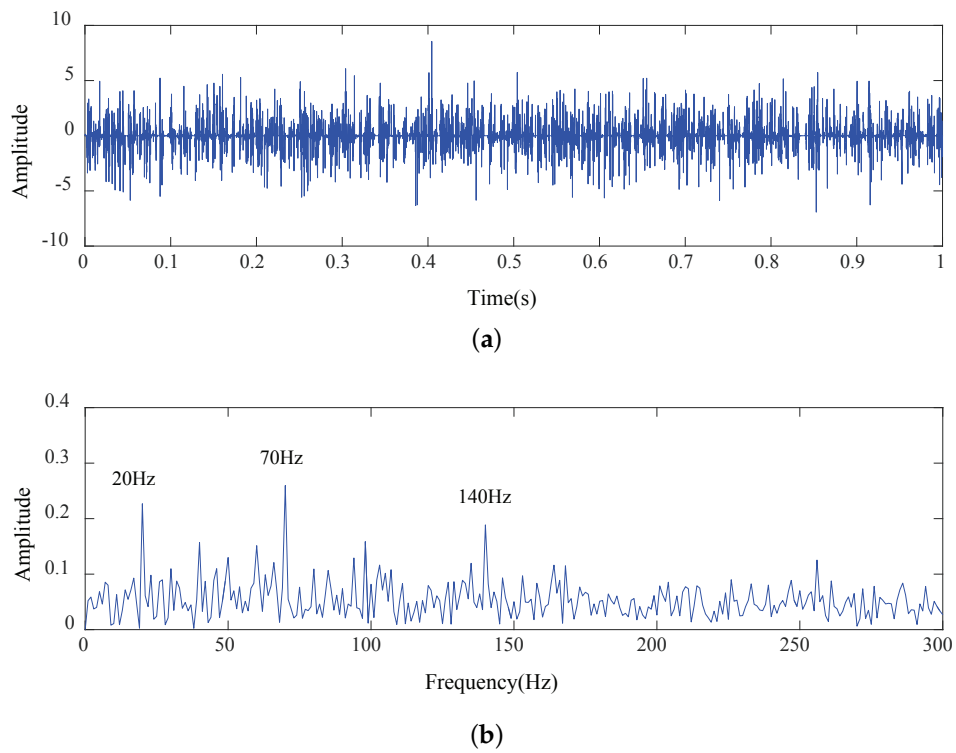


Figure 10. Results of OGS: (a) Time-domain waveform. (b) Frequency spectrum.

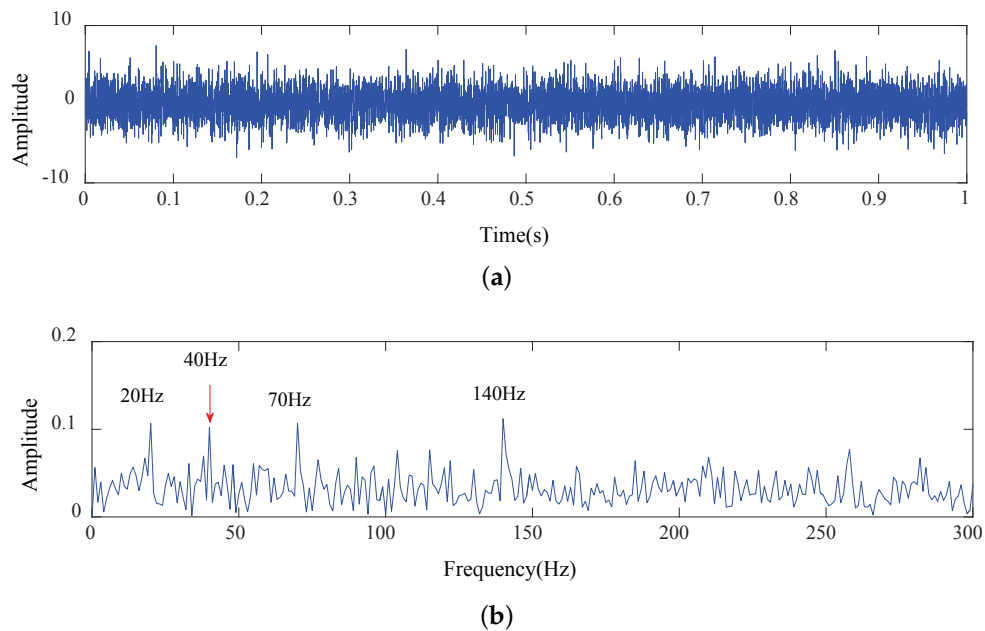


Figure 11. Results of soft threshold: (a) Time-domain waveform. (b) Frequency spectrum.

5. Experimental Verification

In the part of experimental verification, two different signal types are used: (1) Two fault signals collected separately are synthesized to generate composite fault signal. (2) The inner and outer race of a rolling bearing are set with faults respectively, and the fault signal is collected by a single-channel sensor.

5.1. Application to a Synthesized Signal Mixture

Rolling bearing data were taken from the Case West Reserve University (CWRU) [37], wherein inner and outer races each had a single point fault generated by electro-discharge machining, and the experimental platform is shown in Figure 12. The fault sizes of the inner race and outer race were 0.007 inch (width) \times 0.011 inch (depth). The motor speed was 1797 rpm (29.95 Hz), the sampling frequency was 12,000 Hz, and the number of sampling points was 12,000. The type of rolling bearing was SKF62055, and its structural parameters are shown in Table 2. According to the structural parameters of the rolling bearing, the characteristic frequencies of rolling bearing can be calculated; characteristic frequencies of the outer and inner races are about 162.2 Hz and 107.4 Hz respectively. The mixed signal was synthesized by the superposition matrix for the inner and outer race fault data of Case West Reserve University. In order to further weaken the fault characteristics, the inner and outer faults were superimposed with -5 dB noise. Figure 13 shows the time-domain waveform and frequency spectra of the inner race fault, outer race fault, and mixed signal. In the envelope spectrum of the mixed signal Figure 13f, the characteristic frequency of inner race 107.4 Hz can be extracted. However, the characteristic frequency of outer race and its harmonic components cannot be observed.

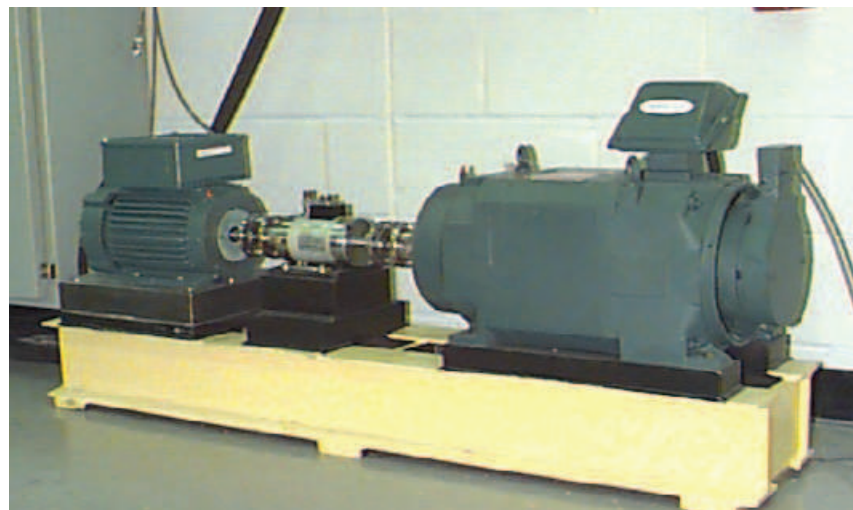
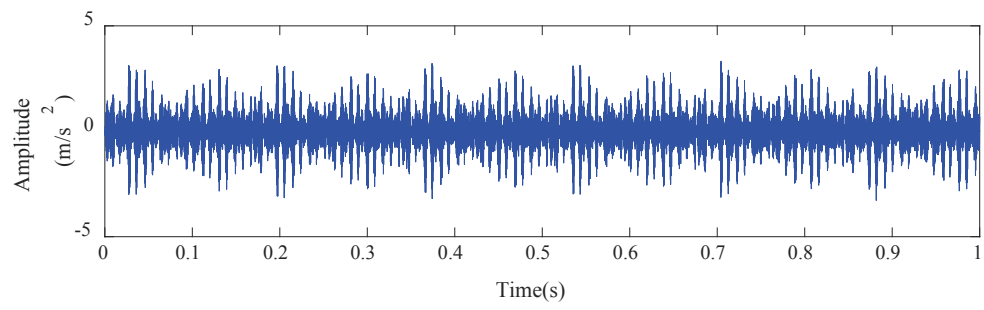


Figure 12. Experimental setup.

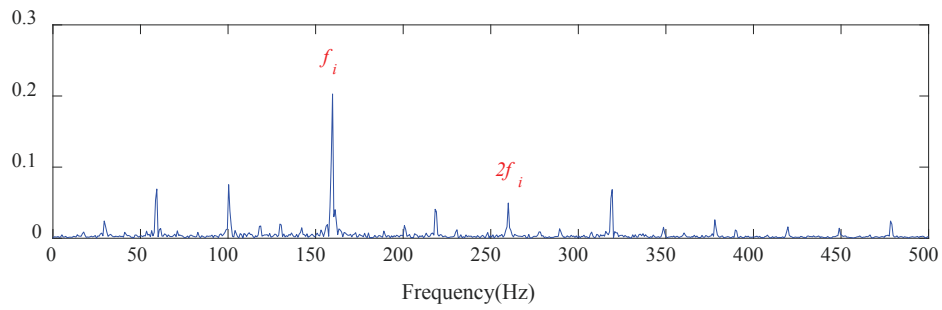
Table 2. Structural parameters of rolling bearing.

Type	Diameter of Balls	Pitch Diameter	Pitch Diameter	Contact Angle
SKF62055	7.94 (mm)	39.04 (mm)	9 (mm)	0° (°)

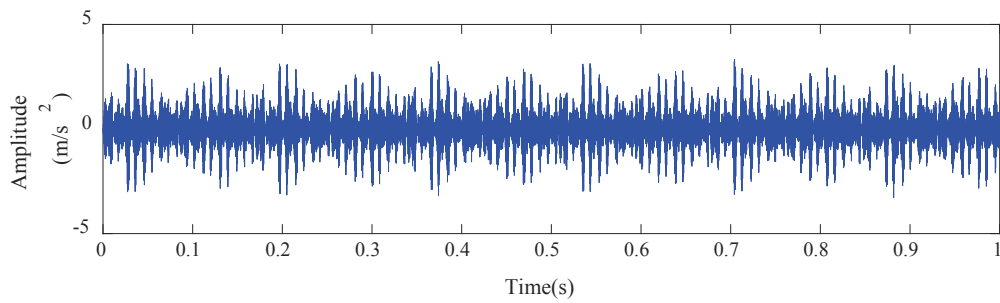
Figure 14 shows the denoised results based on the proposed WOGS algorithm with a group size 6×3 . In the envelope spectrum, Figure 14b, the characteristic frequencies of inner and outer race faults are clearly extracted. Thus, the fault features of the two defects are clearly revealed by the proposed algorithm. We adopt TQWT, OGS, and the soft threshold algorithm for the same synthesized signal for improved verification and comparison. The denoised results are shown in Figures 15–17, where the characteristic frequencies and its harmonics are not obvious. Similarly, R_f and T_f are used for comparative analysis of four algorithms, and the results are shown in Table 3. It can be seen from the table that the energy ratio of WOGS algorithm is the largest, and the CPU running time of soft threshold noise reduction is the shortest.



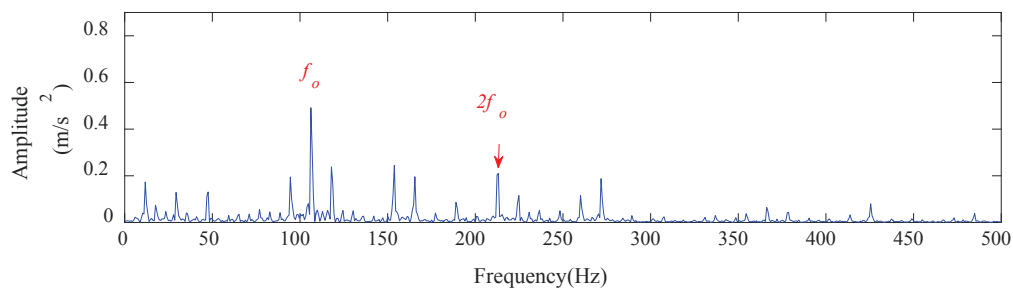
(a)



(b)



(c)



(d)

Figure 13. Cont.

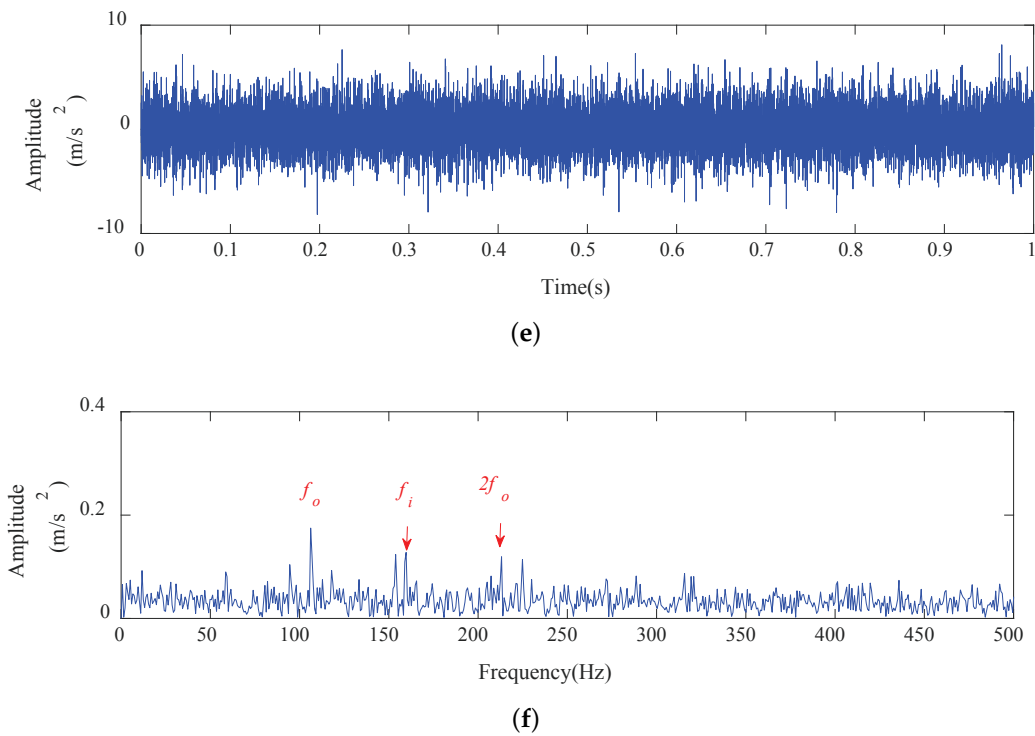


Figure 13. Time-domain waveform and frequency spectrum of the single fault signals and the mixed signal: (a) Time-domain waveform of inner race fault signal. (b) Envelope spectrum of inner race fault signal. (c) Time-domain waveform of outer race fault signal. (d) Envelope spectrum of outer race fault signal. (e) Time-domain waveform of the mixed signal. (f) Envelope spectrum of the mixed signal.

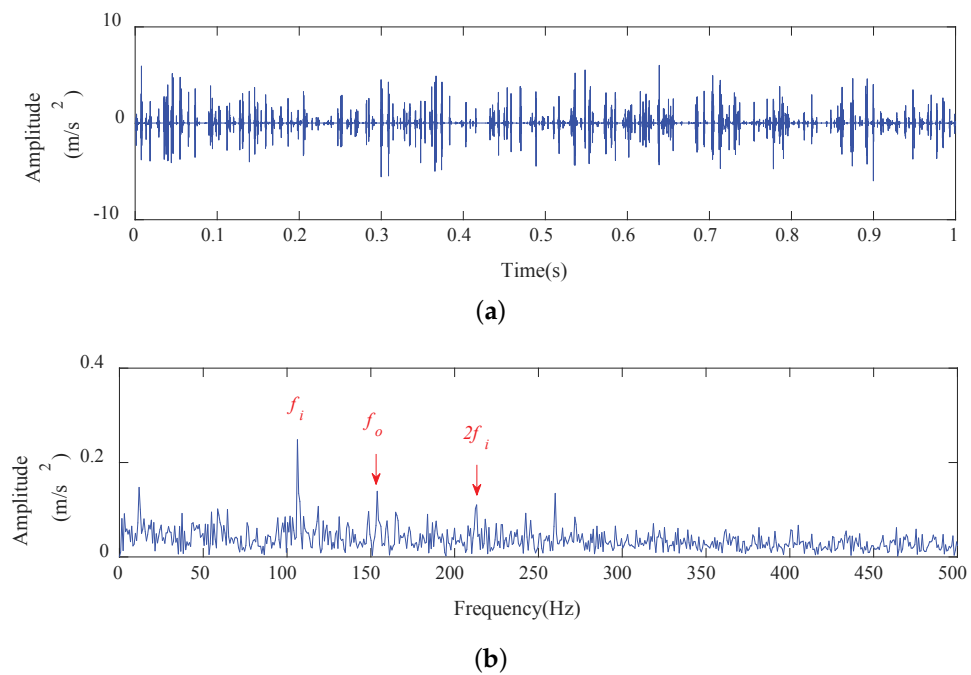


Figure 14. Results of the proposed weighted WOGS algorithm: (a) Time-domain waveform. (b) Envelope spectrum.

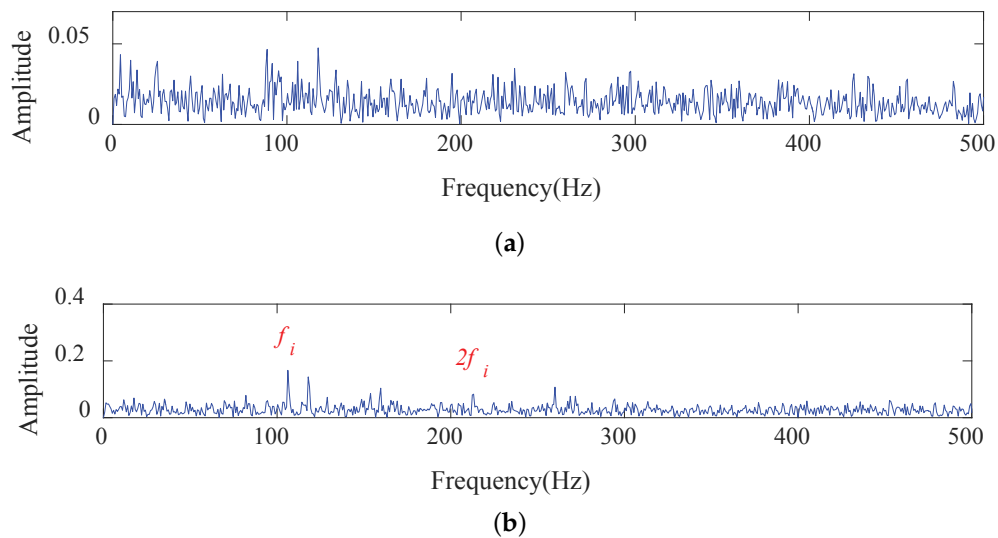


Figure 15. Results of TQWT: (a) High oscillatory component. (b) Low oscillatory component.

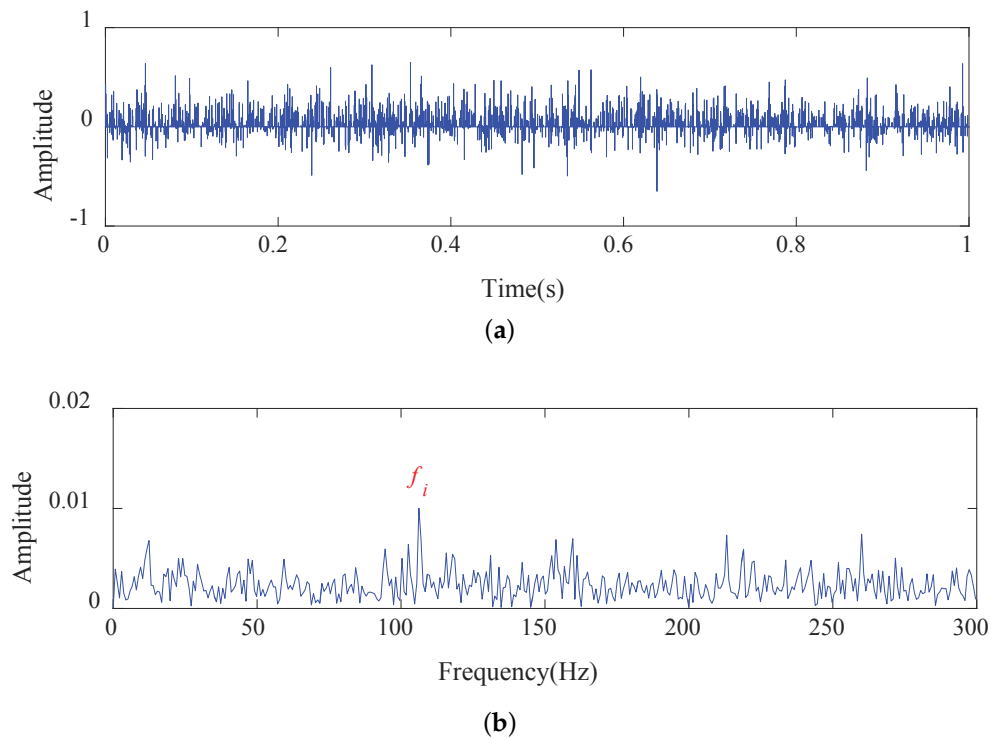


Figure 16. Results of soft threshold: (a) Time-domain waveform. (b) Envelope spectrum.

Table 3. Comparison of R_f and T_f of four algorithms.

Algorithms	R_f	T_f
TQWT	0.0143	2.25 (s)
OGS	0.0194	1.43 (s)
Soft threshold	0.0143	0.51 (s)
WOGS	0.0553	1.48 (s)

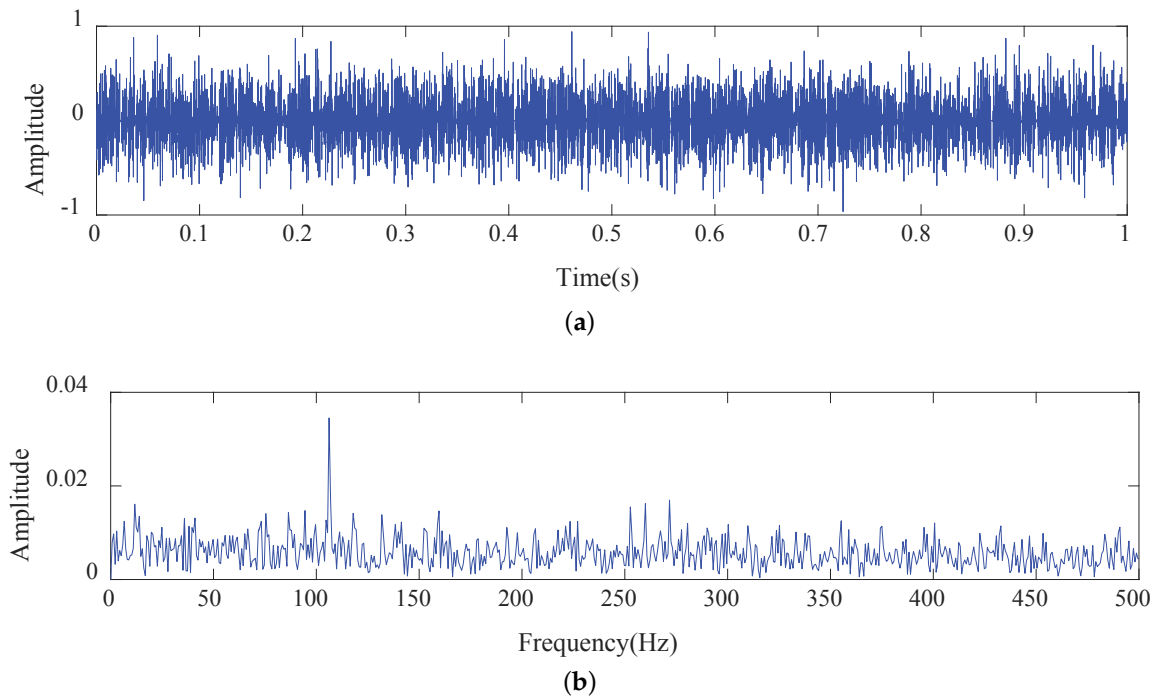
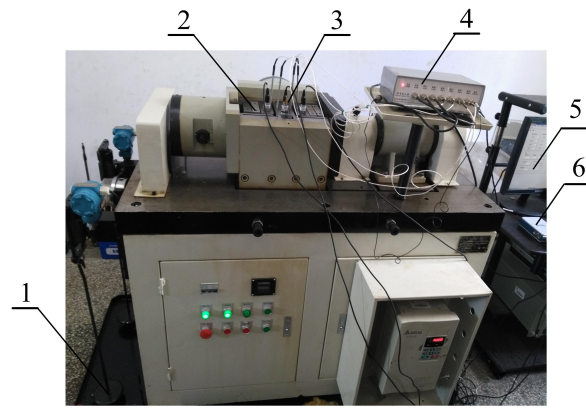


Figure 17. Results of OGS: (a) Time-domain waveform. (b) Envelope spectrum.

5.2. Application to a Real Signal Mixture

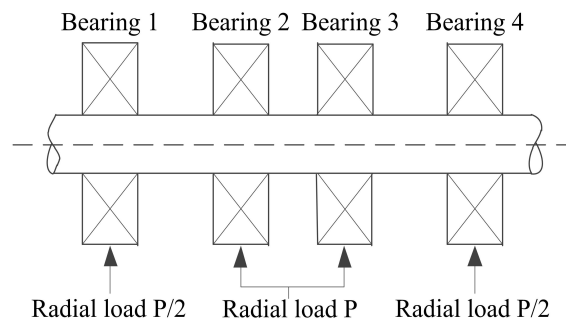
While Section 4 describes the effectiveness of the proposed WOGS algorithm with simulated signal, this section deals with the proposed algorithm used to extract the multiple faults of rolling bearings with a test bench (Figure 18a). The test bench is driven by an AC motor via a shaft and composed of a loading system, four rolling bearings, a sensor monitoring system, a signal modulate circuit, and a software monitoring system. Figure 18b shows the loading diagram of four bearings in the test bench. The sensor monitoring system contains three accelerometers, and four thermocouple sensors are installed on the housing of the rolling bearings to collect bearing vibration and temperature signals. Figure 18c depicts the sensor arrangement. The employed accelerometer, i.e., PCB Piezotronics model 608A11, is used to measure the radial vibration signal, with a nominal sensitivity of 100 mV/g and a measurement range of ± 50 g. NI 9234 is employed for data acquisition, which can simultaneously collect four channels of acceleration signal, and each channel has its own current source to supply the acceleration sensor. The motor speed is 1050 r/min, the signal sampling frequency is 10,240 Hz, and the sampling time is 1 s. Four rolling bearings are mounted on the shaft (Figure 18b). The faulty bearing is equipped on the far left, and the other three positions are mounted with healthy bearings. The type of the experimental bearing is a single row deep groove ball bearing 6205.

One rolling bearing is damaged with an electrical discharge from a wire to simulate a faulty bearing (Figure 19). The inner fault size is 1.6 mm (width) \times 4 mm (depth), and the outer fault size is 1.6 mm (width) \times 2 mm (depth). Table 3 shows the structural parameters of the rolling bearing 6205. According to the calculations of the fault feature frequencies of rolling bearings, the theoretical results of rolling bearing’s characteristic frequencies are shown in Table 4.

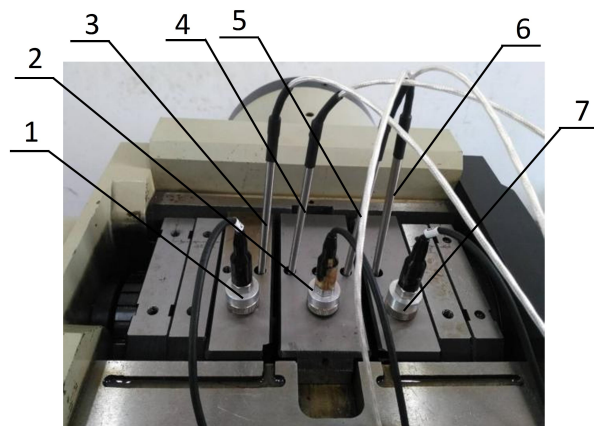


1-loading weight, 2-bearing drive system, 3-sensors, 4-signal modulate device, 5-software monitoring system, 6-NI9234

(a)



(b)



1-accelerometer①, 2-accelerometer②, 3-thermocouple①, 4-thermocouple②, 5-thermocouple③, 6-thermocouple④, 7-accelerometer③

(c)

Figure 18. Rolling bearing test rig: (a) Bearing failure test bench. (b) The diagram of loading system. (c) Sensor layout.



Figure 19. Experimental bearing with multiple faults on the surfaces of the inner race and outer race.

Table 4. The theoretical calculation result of characteristic frequencies of rolling bearing 6205.

Bearing Type	f_i	f_o	f_b	f_c
HRB 6205	94.76 (Hz)	62.74 (Hz)	41.2 (Hz)	6.95 (Hz)

Figure 20a shows the time domain waveform of the collected vibration signal, which is dominated by impulse features. However, determining the time interval of the periodic impulse features is difficult. Figure 20b shows the frequency spectrum corresponding to Figure 20a. The weak multiple fault characteristics of rolling bearings are difficult to extract directly from the frequency spectrum due to the strong background noise. Figure 20c shows the envelope spectrum. Extracting the fault feature frequencies of inner and outer rings is difficult because the multiple fault information may be mixed with noise.

The proposed WOGS algorithm is used to process the experimental signal, with the group size 3×7 . Figure 15 shows the denoised results, and Figure 21a depicts that impulse features are apparent. Moreover, Figure 21b shows the frequency spectrum of denoised signals. It reduces wideband noise, such as white noise. From the envelope spectrum shown in Figure 21c, the frequency components at 63, 134, and 201 Hz have the largest magnitudes, and these frequencies are approximately equal to the outer fault feature frequency and its harmonic frequencies. The frequency components at 95 and 190 Hz are close to the inner fault feature frequency. The result is consistent with the setup of the experiment when outer and inner race faults are extracted.

For comparison, the same experimental signal is analyzed with TQWT, OGS, and soft threshold denoising to further demonstrate the superiority of the proposed algorithm, respectively. The analyzed results are shown in Figures 22–24, and the weak, multiple faults are not more obvious than the results in Figure 21. Similarly, the energy ratio and CPU running time are used to compare and analyze the above algorithms, and the results are shown in Table 5. It can be seen from the table that the energy ratio of the proposed algorithm is obviously larger than in other algorithms. The conclusions drawn are basically consistent with the simulation analysis.

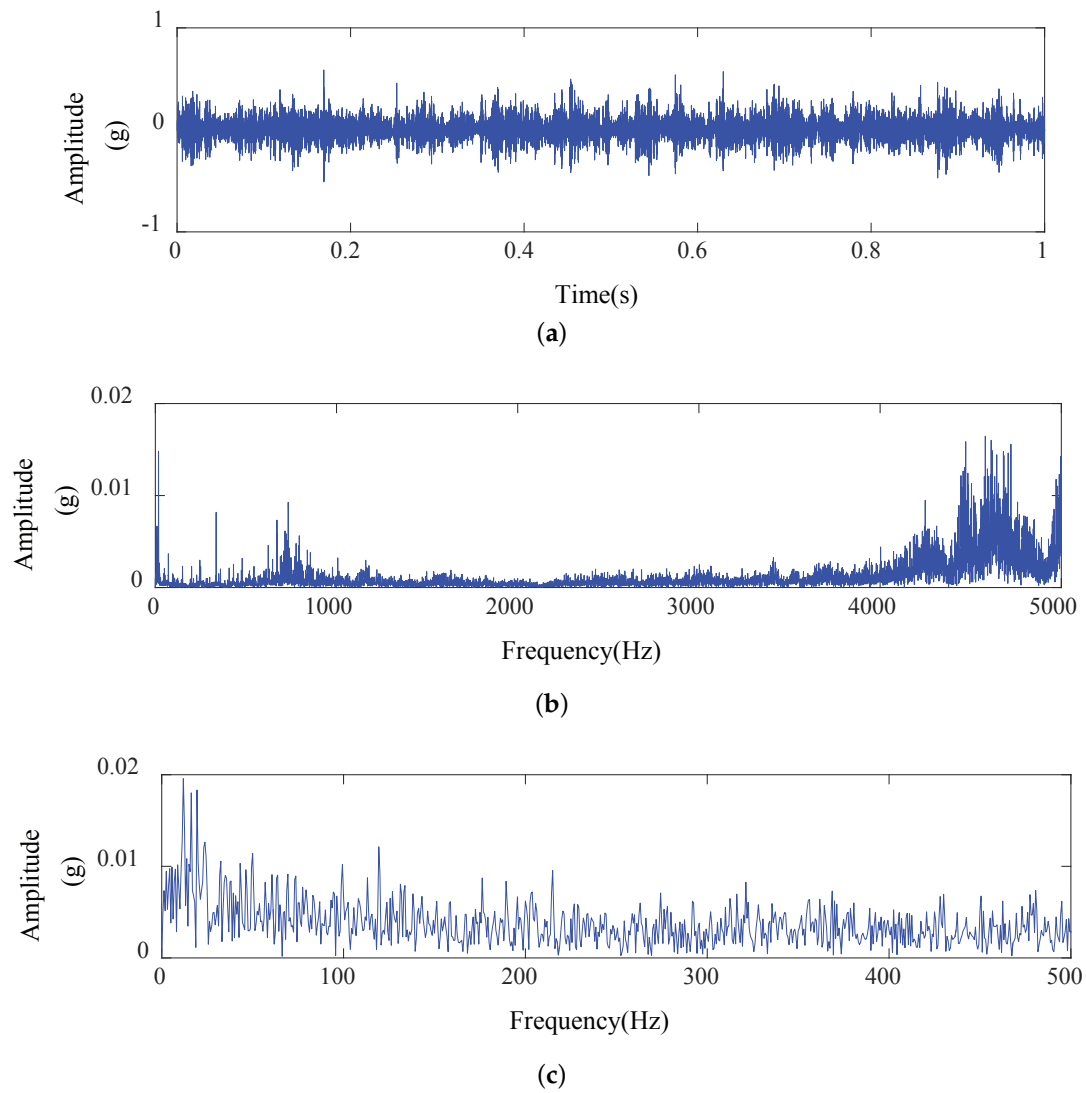


Figure 20. Experimental signal: (a) Time domain waveform. (b) Frequency spectrum. (c) Envelope spectrum.

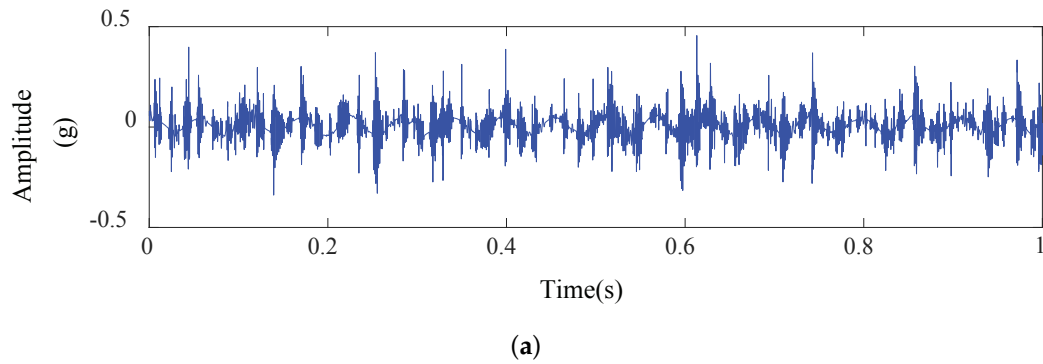


Figure 21. Cont.

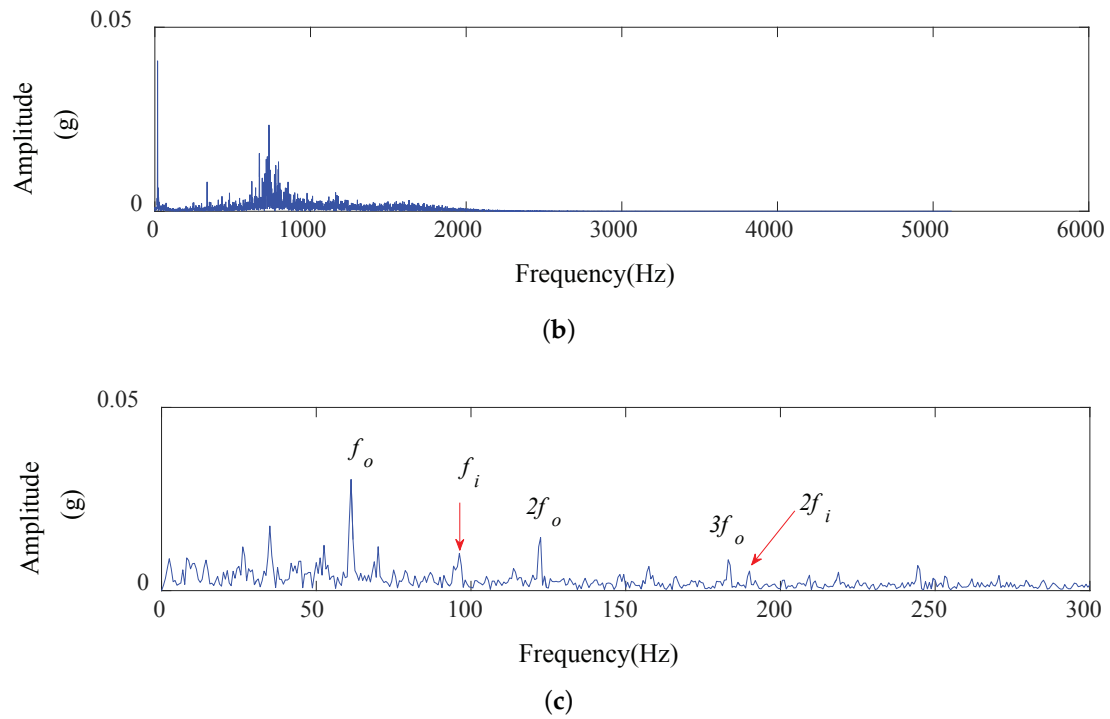


Figure 21. Results of the proposed WOGS algorithm: (a) Time domain waveform. (b) Frequency spectrum. (c) Envelope spectrum.

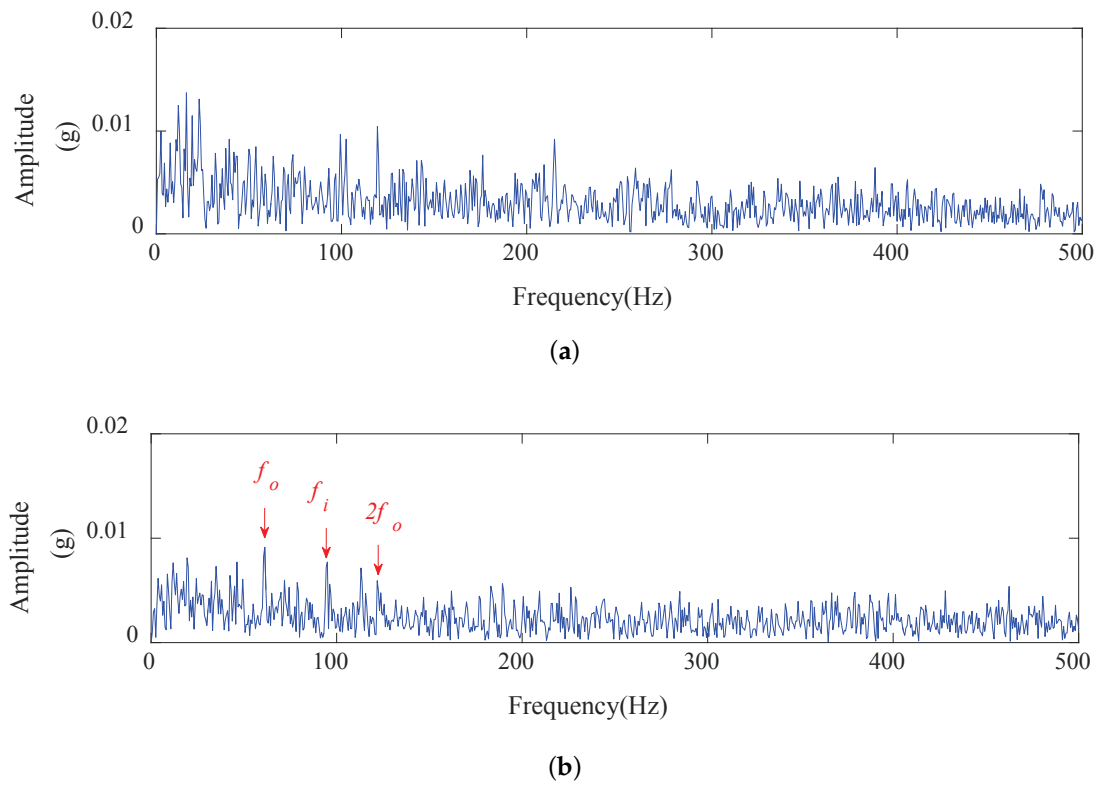


Figure 22. Cont.

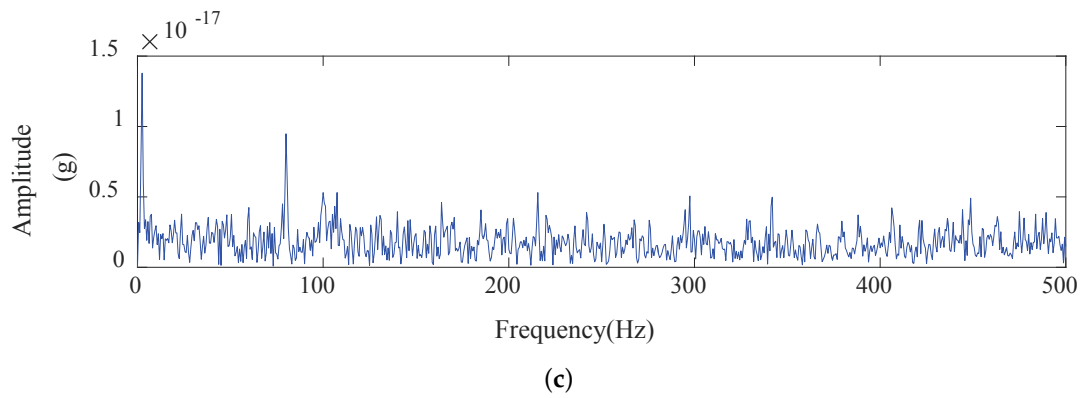


Figure 22. Results of TQWT: (a) High oscillatory component. (b) Low oscillatory component. (c) Residual component.

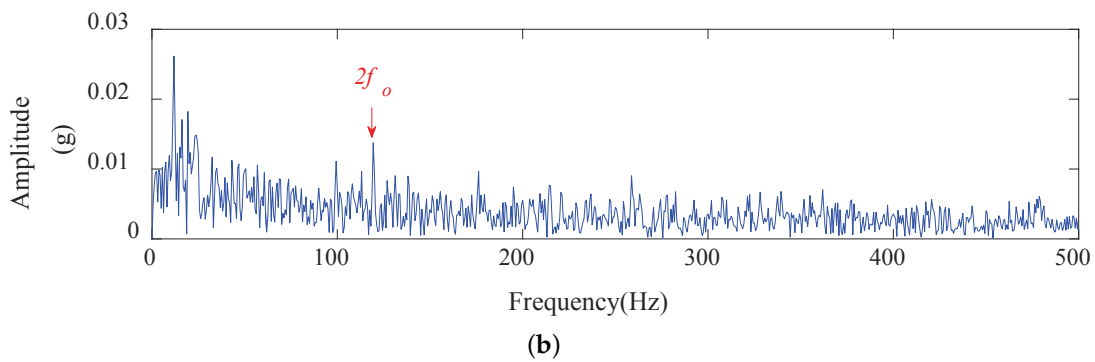
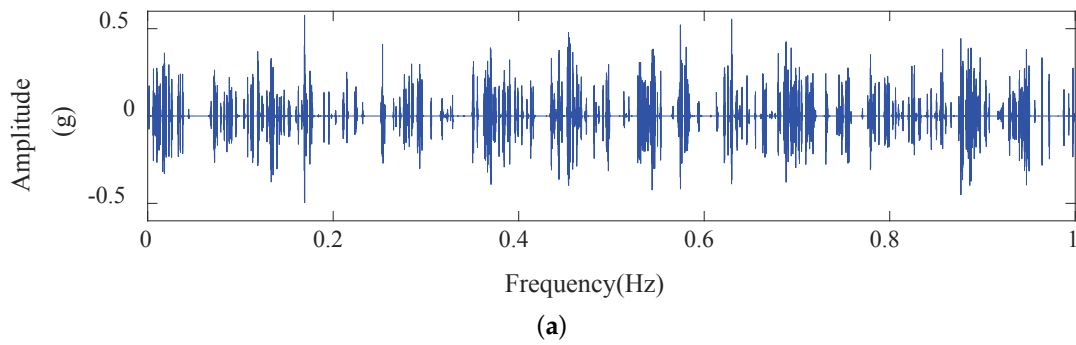


Figure 23. Results of OGS: (a) Time domain waveform. (b) Envelope spectrum.

Table 5. Comparison of R_f and T_f of four algorithms.

Algorithms	R_f	$T_f(s)$
TQWT	0.0185	2.26
OGS	0.023	1.43
Soft threshold	0.0252	0.19
WOGS	0.135	1.20

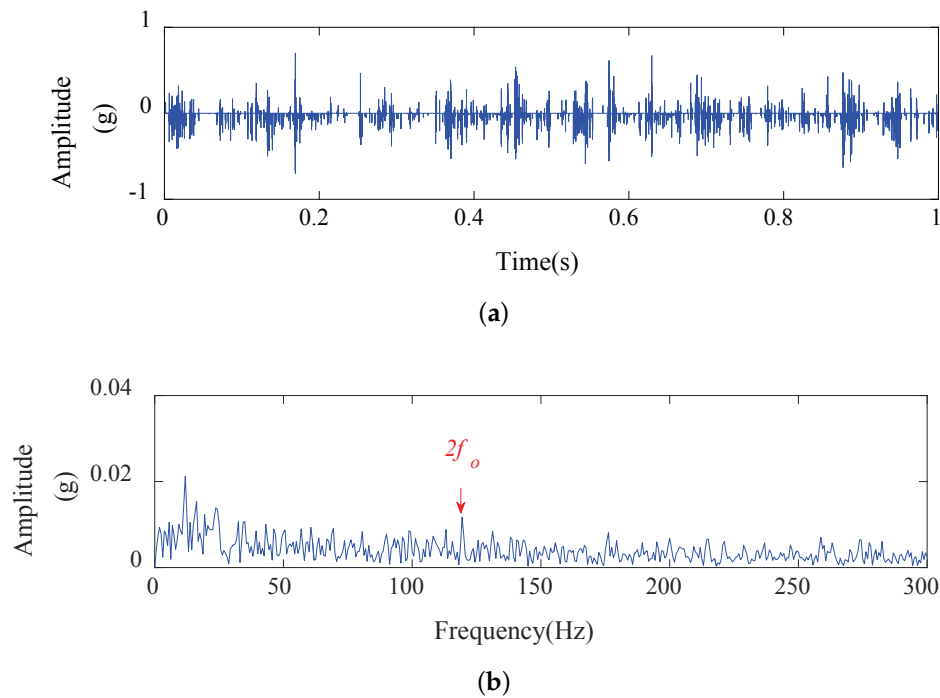


Figure 24. Results of soft threshold: (a) Time domain waveform. (b) Envelope spectrum.

6. Conclusions

This paper presents a weak multiple fault detection algorithm for rolling bearings on the basis of WOGS. The proposed algorithm addresses the problem of weak multiple fault extraction due to the long signal transmission path. The application of the WOGS algorithm to the weak multiple fault diagnosis of rolling bearings demonstrates its validity. The conclusions of this paper are summarized as follows:

- (1) This paper proves that the proposed WOGS algorithm can diagnose weak multiple faults without any prior knowledge like OGS does with some prior knowledge.
- (2) A weighted WOGS is adaptively constructed by analyzing the salient features of the signals—an effective way to enhance impulse characteristics and suppress noise components in the vibration signal.
- (3) The simulation and the experiment performed and the results obtained show that the proposed WOGS algorithm achieves good results in the area of the weak multiple fault diagnosis of rolling bearings, especially regarding a multiple fault signal due to signal attenuation caused by a long transmission path.

In future research, we will continue to explore how to select group structure parameters $K1$ and $K2$ in the WOGS algorithm to obtain better extraction results. In addition, the complexity of the algorithm needs to be simplified to further improve algorithm's efficiency.

Author Contributions: All the authors contributed to all aspects of the manuscript. All authors have read and agreed to the published version of the manuscript.

Funding: This research was supported by the National Natural Science Foundation of China under grant number 51675098, and this paper was also supported by Scientific Research Fund of Nanjing University of Information Science and Technology (number 2018r085#).

Conflicts of Interest: The authors declare no conflict of interest.

Abbreviations

The following abbreviations are used in this manuscript:

WOGS	weighted Morlet wavelet-overlapping group sparse
EMD	Empirical mode decomposition
EEMD	Ensemble empirical mode decomposition
MM	Majorization-minimization
2-D	Two-dimensional
TQWT	Tunable Q-factor wavelet transform

References

- Zeng, M.; Chen, Z. SOSO Boosting of the K-SVD Denoising Algorithm for Enhancing Fault-Induced Impulse Responses of Rolling Element Bearings. *IEEE Trans. Ind. Electron.* **2020**, *67*, 1282–1292. [[CrossRef](#)]
- Yu, D.; Cheng, J.; Yang, Y. Application of EMD method and Hilbert spectrum to the fault diagnosis of roller bearings. *Mech. Syst. Signal Pr.* **2005**, *19*, 259–270. [[CrossRef](#)]
- Antoni, J.; Randall, R.B. The spectral kurtosis: Application to the vibratory surveillance and diagnostics of rotating machines. *Mech. Syst. Signal Pr.* **2006**, *20*, 308–331. [[CrossRef](#)]
- Zhang, W.; Jia, M.P.; Yan, X.A.; Zhu, L. Weighted sparsity-based denoising for extracting incipient fault in rolling bearing. *J. Mech. Sci. Technol.* **2017**, *31*, 4557–4567. [[CrossRef](#)]
- Lau, E.C.C.; Ngan, H.W. Detection of motor bearing outer raceway defect by wavelet packet transformed motor current signature analysis. *IEEE Trans. Instrum. Meas.* **2010**, *59*, 2683–2690. [[CrossRef](#)]
- Kang, M.; Kim, J.; Kim, J.M. An FPGA-based multicore system for real-time bearing fault diagnosis using ultrasampling rate AE signals. *IEEE Trans. Ind. Electron.* **2015**, *62*, 2319–2329. [[CrossRef](#)]
- Cheng, J.; Yu, D.; Tang, J.; Yang, Y. Application of frequency family separation method based upon EMD and local Hilbert energy spectrum method to gear fault diagnosis. *Mech. Mach. Theory* **2008**, *43*, 712–723. [[CrossRef](#)]
- Cheng, J.; Yu, D.; Tang, J.; Yang, Y. Local rub-impact fault diagnosis of the rotor systems based on EMD. *Mech. Mach. Theory* **2009**, *44*, 784–791. [[CrossRef](#)]
- Peng, Z.K.; Chu, F.L. Application of the wavelet transform in machine condition monitoring and fault diagnostics: A review with bibliography. *Mech. Syst. Signal Pr.* **2004**, *18*, 199–221. [[CrossRef](#)]
- Yan, R.; Gao, R.X.; Chen, X. Wavelets for fault diagnosis of rotary machines: A review with applications. *Signal Process.* **2014**, *96*, 1–15. [[CrossRef](#)]
- Wang, L.; Liu, Z.; Miao, Q.; Zhang, X. Time–frequency analysis based on ensemble local mean decomposition and fast kurtogram for rotating machinery fault diagnosis. *Mech. Syst. Signal Pr.* **2018**, *103*, 60–75. [[CrossRef](#)]
- Lei, Y.; Qiao, Z.; Xue, X.; Lin, J.; Niu, S. An underdamped stochastic resonance method with stable-state matching for incipient fault diagnosis of rolling element bearings. *Mech. Syst. Signal Pr.* **2017**, *94*, 148–164. [[CrossRef](#)]
- Li, Y.; Liang, X.; Zuo, M.J. Diagonal slice spectrum assisted optimal scale morphological filter for rolling element bearing fault diagnosis. *Mech. Syst. Signal Pr.* **2017**, *85*, 146–161. [[CrossRef](#)]
- Jiang, H.; Li, C.; Li, H. An improved EEMD with multiwavelet packet for rotating machinery multi-fault diagnosis. *Mech. Syst. Signal Pr.* **2013**, *36*, 225–239. [[CrossRef](#)]
- Chen, J.; Zi, Y.; He, Z.; Li, H. Compound faults detection of rotating machinery using improved adaptive redundant lifting multiwavelet. *Mech. Syst. Signal Pr.* **2013**, *38*, 36–54. [[CrossRef](#)]
- Zhang, D.; Yu, D. Multi-fault diagnosis of gearbox based on resonance-based signal sparse decomposition and comb filter. *Measurement* **2017**, *103*, 361–369. [[CrossRef](#)]
- Du, Z.; Chen, X.; Zhang, H.; Zhang, H.; Yan, R. Sparse Feature Identification Based on Union of Redundant Dictionary for Wind Turbine Gearbox Fault Diagnosis. *IEEE Trans. Ind. Electron.* **2015**, *62*, 6594–6605. [[CrossRef](#)]
- Qin, Y. A New Family of Model-Based Impulsive Wavelets and Their Sparse Representation for Rolling Bearing Fault Diagnosis. *IEEE Trans. Ind. Electron.* **2018**, *65*, 2716–2726. [[CrossRef](#)]
- Wang, Y.; Xiang, J.; Mo, Q.; He, S. Compressed sparse time–frequency feature representation via compressive sensing and its applications in fault diagnosis. *Measurement* **2015**, *68*, 70–81. [[CrossRef](#)]

20. He, G.; Ding, K.; Lin, H. Fault feature extraction of rolling element bearings using sparse representation. *J. Sound Vib.* **2016**, *366*, 514–527. [[CrossRef](#)]
21. Chen, X.; Du, Z.; Li, J.; Li, X.; Zhang, H. Compressed sensing based on dictionary learning for extracting impulse components. *Signal Process.* **2014**, *96*, 94–109. [[CrossRef](#)]
22. Zhipeng, F.; Liang, M. Complex signal analysis for planetary gearbox fault diagnosis via shift invariant dictionary learning. *Measurement* **2016**, *90*, 382–395.
23. Yang, H.; Mathew, J.; Ma, L. Fault diagnosis of rolling element bearings using basis pursuit. *Mech. Syst. Signal Pr.* **2005**, *19*, 341–356. [[CrossRef](#)]
24. Feng, Z.; Chu, F. Application of atomic decomposition to gear damage detection. *J. Sound Vib.* **2007**, *302*, 138–151. [[CrossRef](#)]
25. Liu, B.; Ling, S.F.; Gribonval, R. Bearing failure detection using matching pursuit. *NDT E Int.* **2002**, *35*, 255–262. [[CrossRef](#)]
26. Chen, C.; Huang, J. The benefit of tree sparsity in accelerated MRI. *Med. Image Anal.* **2014**, *18*, 834–842. [[CrossRef](#)]
27. Rao, N.; Shah, P.; Wright, S. Forward–Backward Greedy Algorithms for Atomic Norm Regularization. *IEEE Trans. Signal Proces.* **2015**, *63*, 5798–5811. [[CrossRef](#)]
28. Baldassarre, L.; Bhan, N.; Cevher, V.; Kyriillidis, A.; Satpathi, S. Group-Sparse Model Selection: Hardness and Relaxations. *IEEE Trans. Inform. Theory* **2016**, *62*, 6508–6534. [[CrossRef](#)]
29. Liu, J.; Cui, L.; Luo, X. Survey on Group Sparse Models and Algorithms. *Acta Electron. Sin.* **2015**, *43*, 776–782.
30. Liu, J.; Cui, L.; Luo, X. Structured Sparse Models. *Chin. J. Comput.* **2017**, *40*, 1309–1337.
31. Kowalski, M.; Torr sani, B. Sparsity and persistence: Mixed norms provide simple signal models with dependent coefficients. *Signal Image Video Process.* **2009**, *3*, 251–264. [[CrossRef](#)]
32. Chen, P.; Selesnick, I.W. Group-Sparse Signal Denoising: Non-Convex Regularization, Convex Optimization. *IEEE Trans. Signal Proces.* **2014**, *62*, 3464–3478. [[CrossRef](#)]
33. He, W.; Ding, Y.; Zi, Y.; Selesnick, I.W. Sparsity-based algorithm for detecting faults in rotating machines. *Mech. Syst. Signal Pr.* **2016**, *72–73*, 46–64. [[CrossRef](#)]
34. He, W.; Ding, Y.; Zi, Y.; Selesnick, I.W. Repetitive transients extraction algorithm for detecting bearing faults. *Mech. Syst. Signal Pr.* **2017**, *84*, 227–244. [[CrossRef](#)]
35. Figueiredo, M.A.; Bioucas-Dias, J.M.; Nowak, R.D. Majorization-minimization algorithms for wavelet-based image restoration. *IEEE Trans. Image Process.* **2007**, *16*, 2980–2991. [[CrossRef](#)]
36. Chen, P.; Selesnick, I. Translation-invariant shrinkage/thresholding of group sparse signals. *Signal Process.* **2014**, *94*, 476–489. [[CrossRef](#)]
37. Case Western Reserve University Bearing Data Center. Available online: <https://csegrouops.case.edu/bearingdatacenter/home> (accessed on 11 March 2020).

